Supplement of Nat. Hazards Earth Syst. Sci., 26, 1935–1954, 2026
https://doi.org/10.5194/nhess-26-1935-2026-supplement

Supplement of

Assessing extreme total water levels across Europe for large-scale coastal flood analysis

Camila Cotrim et al.

Correspondence to: Alexandra Toimil (toimila@unican.es)

Sea level and wave datasets

This section describes the development and validation of the astronomical tide, storm surge, and wave datasets used in this study.

Astronomical tide

TPXO is a global ocean tide model developed by Oregon State University. It provides a best fit to the Laplace Tidal Equations and along-track averaged data from TOPEX/Poseidon and Jason satellite missions. TPXO is a barotropic model of sea surface elevation and currents that employs a variational assimilation scheme, primarily using satellite altimetry data. The methods used to compute the model are described by Egbert et al. (1994) and further detail is provided by Egbert & Erofeeva (2002).

In this study, we used tidal constituents from the TPXO9 version 5 global tidal model (TPXO9v5). The TPXO9v5 database includes eight primary tidal constituents (M2, S2, N2, K2, K1, O1, P1, Q1), two long-period constituents (Mf, Mm), and three nonlinear harmonic constituents (M4, MS4, MN4). These are provided at a spatial resolution of 1/30° (~3.5 km) near the coast and 1/6° (~16 km) offshore. The physical characteristics of these tidal constituents are then used to reconstruct hourly time series of tide level. The resulting astronomical tide time series are then validated against the tide component from 48 tide gauge records covering all European coasts. The sea level records from the tide gauges were obtained from the GESLA3 (Global Extreme Sea Level Analysis, version 3.0) database (Haigh et al., 2022). A harmonic analysis using the UTide tool (Codiga, 2011) was conducted to isolate the astronomical tide component and the non-tidal residual (NTR) component from the still water level (SWL) record measured by the tide gauges.

The validation was performed using comparisons of time series, quantile–quantile plots, and several statistical metrics (e.g., root mean square error – RMSE, bias, and Pearson correlation). Table S1 presents statistical metrics of the comparison of the tide series simulated from the TPXO9v5 outputs and measured by the tide gauges. Localized examples of quantile-quantile plots are presented in Figure S1. The results show a near-perfect agreement across the validation of the tidal model. With most of the cases presenting a RMSE below 10 cm, bias below 1 cm, and a Pearson correlation above 0.9, the results indicate the series accurately reproduce both the magnitude and phase of tidal cycles through time.

Table S1: Information on the tide-gauge stations used for the validation of the tidal model. Tide-gauge station names, coordinates, RMSE, bias, and Pearson correlation values at each location.

	Tide gauge	Location		RMSE (cm)	Bias (cm)	Correlation
		Latitude	Longitude			
1	Vigo	42.243	-8.726	6.991	-0.563	1.00
2	A Coruña	43.364	-8.399	6.172	-0.610	1.00
3	Ferrol	43.463	-8.326	5.476	-0.611	1.00
4	Gijón	43.558	-5.698	6.269	-0.637	1.00
5	Santander	43.461	-3.791	7.617	-0.644	1.00
6	Bilbao	43.357	-3.05	5.689	-0.644	1.00
7	Barcelona	41.342	2.163	3.851	-0.110	0.78
8	Catania	37.498	15.094	3.487	0.081	0.84
9	Livorno	43.546	10.299	3.817	-0.078	0.90
10	Ancona	43.625	13.506	4.713	-0.268	0.92
11	Imperia	43.878	8.019	3.511	-0.045	0.88
12	Genova	44.41	8.925	3.138	-0.100	0.92
13	Ravenna	44.492	12.283	7.328	-0.435	0.94
14	Venezia	45.418	12.426	7.699	-0.506	0.95
15	Trieste	45.649	13.759	9.318	-0.522	0.94
16	Nice	43.695	7.285	3.123	-0.104	0.91
17	Monaco	43.733	7.424	3.044	-0.104	0.91
18	Port Bloc	45.568	-1.062	17.923	-0.711	0.99
19	La Rochelle	46.148	-1.226	23.011	-1.349	0.99
20	Brest	48.383	-4.495	17.012	-0.905	1.00
21	Cherbourg	49.651	-1.635	11.205	0.181	1.00
22	Calais	50.969	1.868	19.824	1.374	0.99
23	Dunkerque	51.048	2.367	20.374	1.380	0.99
24	St Marys	49.918	-6.315	9.727	-0.281	1.00
25	Newlyn	50.103	-5.543	10.155	-0.133	1.00
26	Cromer	52.934	1.301	10.479	2.369	1.00
27	Whitby	54.483	-0.616	8.525	1.129	1.00
28	North Shields	55.007	-1.439	8.159	1.549	1.00
29	Aberdeen	57.15	-2.083	8.734	1.958	1.00
30	Stornoway	58.207	-6.389	9.017	-0.987	1.00
31	Wick	58.433	-3.083	8.214	0.206	0.99
32	Lerwick	60.154	-1.138	6.509	-0.424	0.99
33	Castletownbere	51.649	-9.903	7.094	-0.338	1.00
34	Malinhead	55.367	-7.333	9.274	-0.823	0.99
35	Cuxhaven	53.868	8.717	46.100	0.140	0.92
36	Helgoland	54.179	7.89	47.125	-0.001	0.85
37	Aarhus	56.15	10.217	8.160	-0.121	0.87
38	Goteborg	57.683	11.8	7.466	0.201	0.59
39	Stockholm	59.325	18.082	1.020	-0.088	0.65
40	Tregde	58.006	7.566	6.147	-0.069	0.72
41	Helgeroa	58.995	9.856	8.320	-0.062	0.69
42	Viker	59.036	10.949	9.111	-0.066	0.67
43	Rorvik	64.867	11.25	32.878	-0.003	0.86
44	Kabelvaag	68.212	14.482	15.806	-0.001	0.98
45	Andenes	69.326	16.135	20.360	-0.002	0.92
46	Vardo	70.333	31.1	58.073	0.004	0.71
47	Honningsvag	70.98	25.973	43.329	-0.002	0.79
48	Reykjavik	64.15	-21.933	7.282	-0.150	1.00

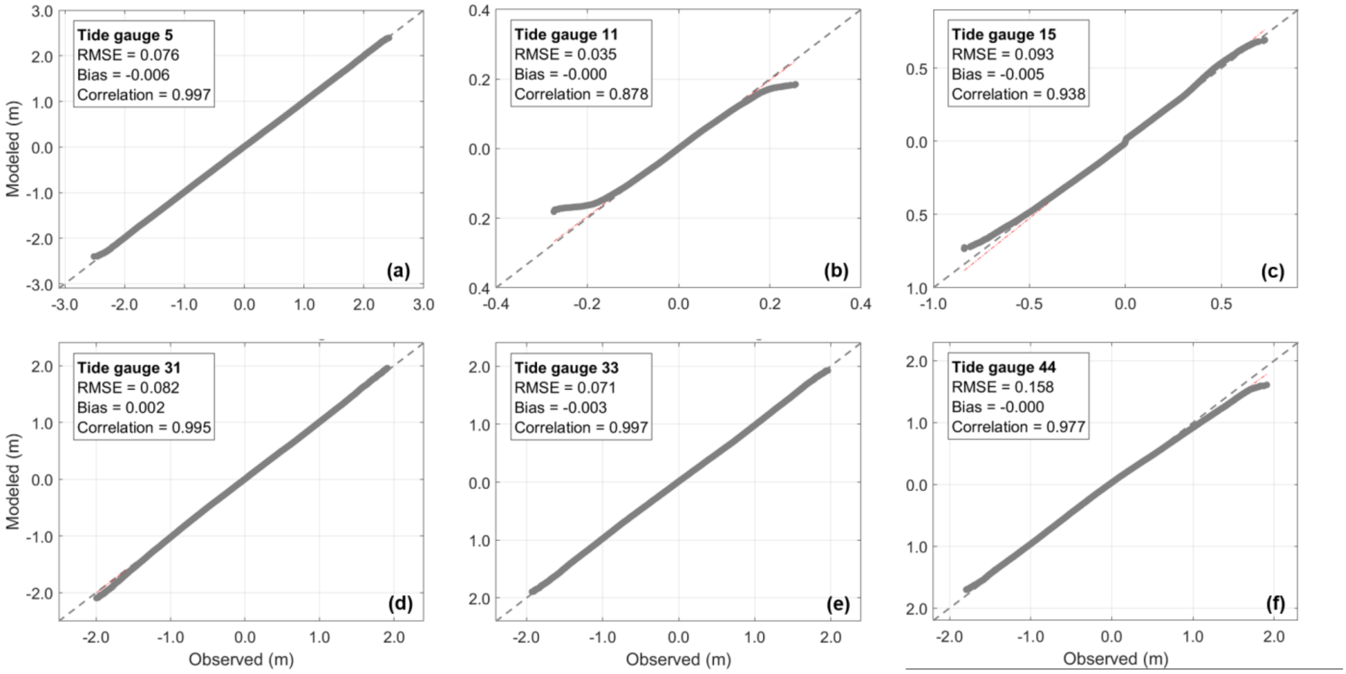

Figure S1: Quantile–quantile plots comparing tide-gauge observations (measured) with the tidal model (modeled) for six locations. Gray dashed lines indicate a 1:1 relationship and red-dashed lines correspond to a linear regression fitted to the paired quantiles. RMSE and bias values are shown in meters. (a) Santander (Spain), (b) Imperia (Italy), (c) Trieste (Italy), (d) Wick (Scotland), (e) Castletownbere (Ireland), and (f) Kabelvaag (Norway).

Storm surge

Storm surge modeling was carried out using the Regional Ocean Modelling System (ROMS), developed by Rutgers University (Shchepetkin and McWilliams, 2005). The model was implemented over a European domain using an orthogonal grid, with a horizontal resolution ranging from 5 to 11 km and a minimum depth of 10 m. The computational domain extended from 30.943°W to 42.943°E in longitude, and from 25.05°N to 72.983°N in latitude, comprising a total of 272,382 grid nodes. The model configuration followed that of Cid et al. (2014). The Chapman scheme (Chapman, 1985) was applied to prescribe the free-surface boundary condition, and the Flather radiation condition (Flather, 1976) was used for the depth-integrated momentum components. Bottom friction was represented using a quadratic drag coefficient of 10^{-4}, and horizontal mixing was parameterized with a constant harmonic viscosity of 500 m^2/s. Hourly fields of surface wind and mean sea level pressure from the ERA5 reanalysis (Hersbach et al., 2020) were used as atmospheric forcing. Sea level boundary conditions were provided by tidal elevations and depth-averaged currents from TPXO9 tidal model, along with the inverse barometer effect from ERA5 mean sea level pressure fields.

To capture the nonlinear interactions between tides and storm surges, a three-step simulation procedure was applied. First, a simulation of the SWLs was performed, in which both tidal and meteorological forcings were included to represent the full coupled dynamics. Second, a tide-only simulation was carried out using tidal constituents as boundary conditions, allowing the astronomical tide to be isolated. Finally, storm surge levels were obtained by subtracting the astronomical tide from the SWL simulation.

Surge elevations were validated against 48 tide-gauge records along the European coasts. The validation between instrumental and numerical data was conducted using comparisons of time series, quantile–quantile plots, scatter plots, and several error metrics (e.g., root mean square error – RMSE, bias, and Pearson correlation). Figure S2 shows the storm surge hindcast and tide-gauge hourly time series over a six-month time window for three tide-gauge stations. Figure S3 shows scatter plots and quantile-quantile plots comparing the modeled surge elevations with the observed NTR from the tide gauges. The 75th, 90th, 95th, and 99.5th quantiles are indicated.

The storm surge hindcast dataset exhibits excellent performance in reproducing the temporal evolution of storm surge events, particularly the peak values observed during storm events. An underestimation of maxima above the 99.5th percentile and an overestimation of minima below the 10th percentile is observed at many tide-gauge stations. These differences between simulated and observed data may be attributed to local effects at the tide-gauge stations, which are often located in estuaries, harbors, or complex coastal areas where the tidal signal is distorted by nearshore processes that cannot be resolved by the spatial resolution of the ROMS grid cells. The underestimation of some storm surge maxima may also result from the ERA5 wind fields, as several studies (e.g., Chen et al., 2024) have reported a systematic underestimation of ERA5 wind speeds during extratropical cyclone events. Table S2 presents statistical metrics of the comparison between modeled and observed storm surge data. The RMSE at most stations is below 10 cm. Biases are consistently below 2 cm, with a systematic underestimation observed along the North Sea coasts.

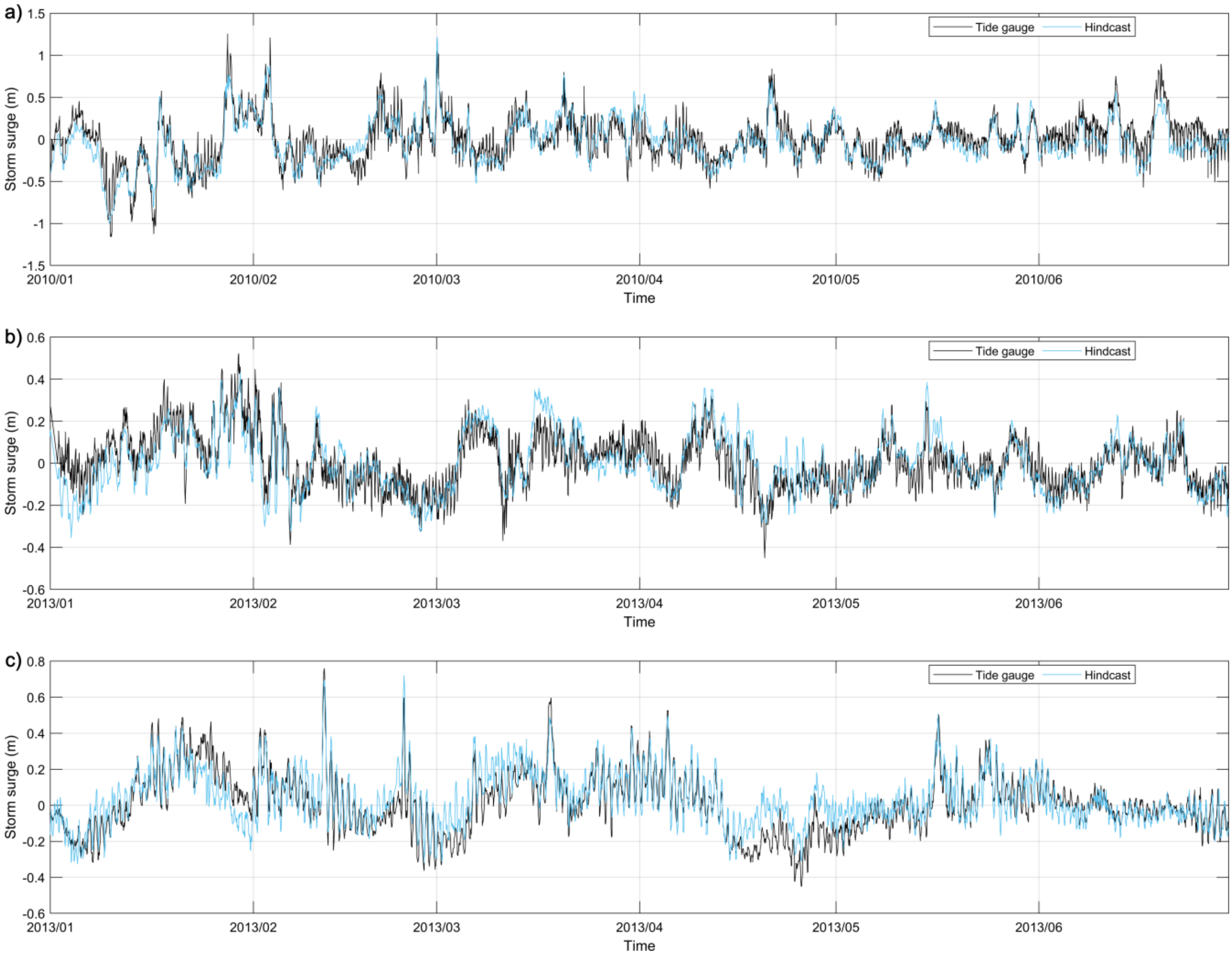

Figure S2: Hourly time series of storm surge from the storm surge hindcast and non-tidal residual sea level from tide-gauge observations. (a) Cuxhaven (Germany), (b) Cherboug (France), and (c) Venice (Italy).

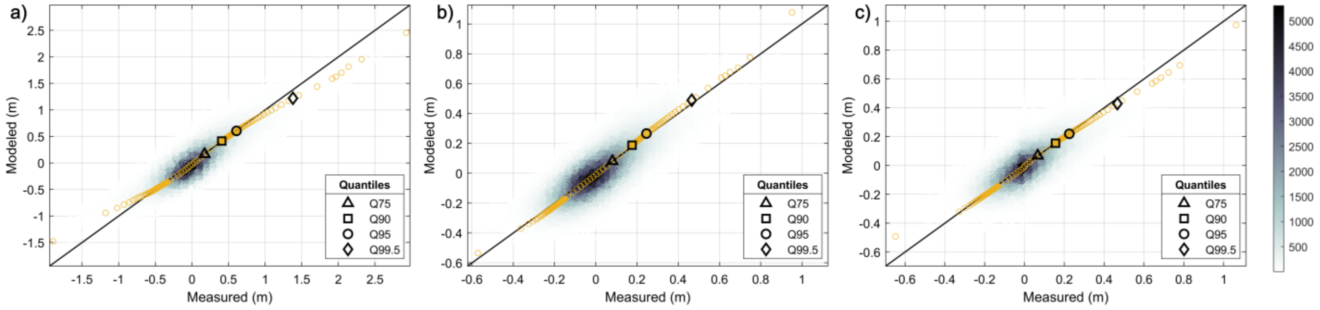

Figure S3: Scatter plot (gray colormap) and quantile–quantile plot (yellow circles and markers) comparing tide-gauge observations (measured) with the storm surge hindcast (modeled). (a) Cuxhaven (Germany), (b) Cherboug (France), and (c) Venice (Italy).

Table S2: Information on the tide-gauge stations used for the validation of the storm surge hindcast. Tide-gauge station names, coordinates, RMSE, bias, and Pearson correlation values at each location.

	Tide gauge	Location		RMSE (cm)	Bias (cm)	Correlation
		Latitude	Longitude			
1	Vigo	42.243	-8.726	7.447	0.023	0.74
2	A Coruña	43.364	-8.399	6.840	-0.073	0.77
3	Ferrol	43.463	-8.326	7.434	0.000	0.78
4	Gijón	43.558	-5.698	7.130	-0.054	0.76
5	Santander	43.461	-3.791	6.732	-0.053	0.72
6	Bilbao	43.357	-3.05	7.124	0.044	0.72
7	Barcelona	41.342	2.163	7.430	0.006	0.69
8	Catania	37.498	15.094	6.193	-0.149	0.63
9	Livorno	43.546	10.299	6.736	-0.351	0.70
10	Ancona	43.625	13.506	8.046	-0.639	0.74
11	Imperia	43.878	8.019	6.087	-0.241	0.71
12	Genova	44.41	8.925	6.105	-0.331	0.73
13	Ravenna	44.492	12.283	8.555	-0.652	0.75
14	Venezia	45.418	12.426	8.989	-0.691	0.74
15	Trieste	45.649	13.759	9.582	-0.523	0.72
16	Nice	43.695	7.285	6.024	-0.234	0.72
17	Monaco	43.733	7.424	5.939	-0.192	0.72
18	Port Bloc	45.568	-1.062	9.130	-0.630	0.72
19	La Rochelle	46.148	-1.226	9.707	-0.628	0.71
20	Brest	48.383	-4.495	8.209	-0.753	0.78
21	Cherbourg	49.651	-1.635	8.678	-0.703	0.78
22	Calais	50.969	1.868	13.121	-0.903	0.74
23	Dunkerque	51.048	2.367	13.277	-1.151	0.77
24	St Marys	49.918	-6.315	7.851	-0.594	0.77
25	Newlyn	50.103	-5.543	8.189	-0.613	0.77
26	Cromer	52.934	1.301	10.326	-1.292	0.87
27	Whitby	54.483	-0.616	8.982	-1.079	0.84
28	North Shields	55.007	-1.439	8.940	-1.074	0.82
29	Aberdeen	57.15	-2.083	8.657	-1.103	0.82
30	Stornoway	58.207	-6.389	9.307	-1.238	0.84
31	Wick	58.433	-3.083	9.002	-1.252	0.83
32	Lerwick	60.154	-1.138	8.383	-1.030	0.82
33	Castletownbere	51.649	-9.903	7.751	-0.564	0.81
34	Malinhead	55.367	-7.333	8.204	-1.219	0.87
35	Cuxhaven	53.868	8.717	16.696	-2.172	0.88
36	Helgoland	54.179	7.89	13.364	-2.319	0.90
37	Aarhus	56.15	10.217	9.878	-0.951	0.81
38	Goteborg	57.683	11.8	10.088	-1.190	0.82
39	Stockholm	59.325	18.082	10.385	-0.363	0.71
40	Tregde	58.006	7.566	8.812	-0.861	0.78
41	Helgeroa	58.995	9.856	9.464	-1.034	0.83
42	Viker	59.036	10.949	10.632	-0.988	0.82
43	Rorvik	64.867	11.25	9.463	-1.176	0.82
44	Kabelvaag	68.212	14.482	9.637	-1.261	0.83
45	Andenes	69.326	16.135	9.576	-0.969	0.78
46	Vardo	70.333	31.1	9.147	-0.820	0.78
47	Honningsvag	70.98	25.973	9.026	-0.940	0.79
48	Reykjavik	64.15	-21.933	7.730	-0.560	0.82

Wind-waves

The offshore wave dataset was obtained from a wave hindcast developed using the third-generation numerical wave model WaveWatchIII (WW3; Tolman, 2009), version 7.00. The wave spectral domain is discretized into 24 directions and 32 nonlinearly spaced frequencies ranging from 0.0373 Hz to 0.7159 Hz, with a frequency increment factor of 1.1. Bathymetry, land-sea masks, and obstruction grids were generated using the WW3 grid generation software (Chawla and Tolman, 2008). The model uses spatial fields of surface wind and sea ice concentration from the ERA5 reanalysis as input. A total of four domains were considered to design the multi-grid configuration of the regional wave hindcast. This configuration included a global regular grid with a spatial resolution of 1/2°, and two irregular (curvilinear) polar stereographic grids with a spatial resolution of 18 km in both directions, following an Irregular–Regular–Irregular (IRI) grid scheme (Rogers and Linzell, 2018). In addition, a regular grid covering the European Atlantic shelf and seas at 1/8° resolution was included. The physical formulation ST4 of Ardhuin et al. (2010) was adopted for wind input and energy dissipation, using the T471 parameterization (WW3DG, 2019). Default parameter values were used, except for the non-dimensional wind-wave growth parameter (β_{max}), which was tuned to calibrate the model for the ERA5 wind fields. The methodology proposed by Stopa (2018), based on satellite altimetry observations, was adopted. The calibrated β_{max} parameter value of 1.46 was used for the simulations.

The DOW method (Camus et al., 2013) was setup and applied to obtain the nearshore wave database along the European coast. The nearshore wave hindcast was developed in four main steps: (i) sixteen unstructured numerical domains were designed to provide wave information at a coastal spatial resolution of 1 km; (ii) a total of 1,000 hourly sea-state cases, representative of both mean and extreme conditions, were selected from the offshore wave hindcast for each numerical domain; (iii) the 1,000 wave conditions were simulated using the SWAN (Simulating Waves Nearshore) model (Booij et al., 1999); and (iv) continuous hourly time series of sea-state parameters at the coastal target points (CTPs) were reconstructed.

The selection of the 1,000 sea states to be propagated nearshore was based on significant wave height, mean period, and mean wave direction from the offshore wave hindcast for the European region, as well as on ERA5 wind fields and sea-ice coverage. The maximum-dissimilarity algorithm was applied over the principal components of these standardized variables to select the simulation cases. SWAN version 41.45 was used to perform the nearshore wave simulations. This version was selected for its improved physical formulations, particularly its ability to activate wave dissipation due to sea ice. Prior to the numerical simulation of the selected cases, the sensitivity of coastal wave conditions to sea level variations was assessed. Based on the results, each selected sea state was propagated at three different water levels in domains with meso- and macro-tidal ranges, resulting in 3,000 simulations per domain.

Finally, a comprehensive validation process was conducted for both the offshore and nearshore components of the wave hindcast. Validation was based on comparisons between the offshore and nearshore hindcast products and buoy observations. Wave buoy records were obtained from the quality-controlled Global Ocean Delayed Mode Wave Product dataset, provided by the Copernicus Marine Environment Monitoring Service (CMEMS). A total of 84 offshore buoys (i.e., farther than 5 km from the coastline) and 109 coastal buoys were selected along the European coast to validate the offshore and nearshore wave databases, respectively. Most of the analyzed buoys cover periods longer than 10-15 years.

Validation results for offshore wave data are shown in Figure S4. The comparison of significant wave height from the hindcast against offshore buoys resulted in an average bias of –0.07 m, RMSE of 0.34 m, and Pearson correlation of 0.93. Bias, RMSE, and Pearson correlation values resulting for the nearshore hindcast compared with coastal buoy observations are shown in Figure S5. The spatial distribution of the bias shows both positive and negative values, which in most locations do not exceed an absolute value of 0.15 m. Positive biases are predominant in the Baltic Sea, while negative biases prevail in the Mediterranean Sea and the Canary Islands. Other regions present a mix of positive and negative values, with several coastal areas showing biases close to zero. RMSE values between 0.2 and 0.3 m are observed in the North Sea, the Baltic Sea, and most locations in the Mediterranean Sea. Higher values are found in the Aegean Sea, Cantabrian Sea, English Channel, and around the British Isles. Pearson correlation coefficients remain above 0.6 for all buoys analyzed, with 85% of the buoys exhibiting values above 0.8.

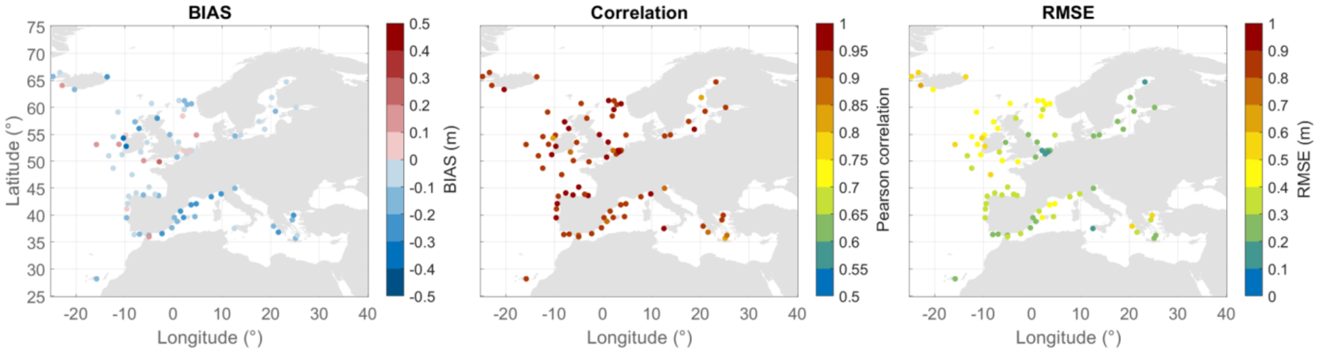

Figure S4: Spatial distribution of bias (left), Pearson correlation (middle), and RMSE (right) in significant wave height (Hs, m) from the offshore wave hindcast, evaluated at the locations of offshore wave buoys.

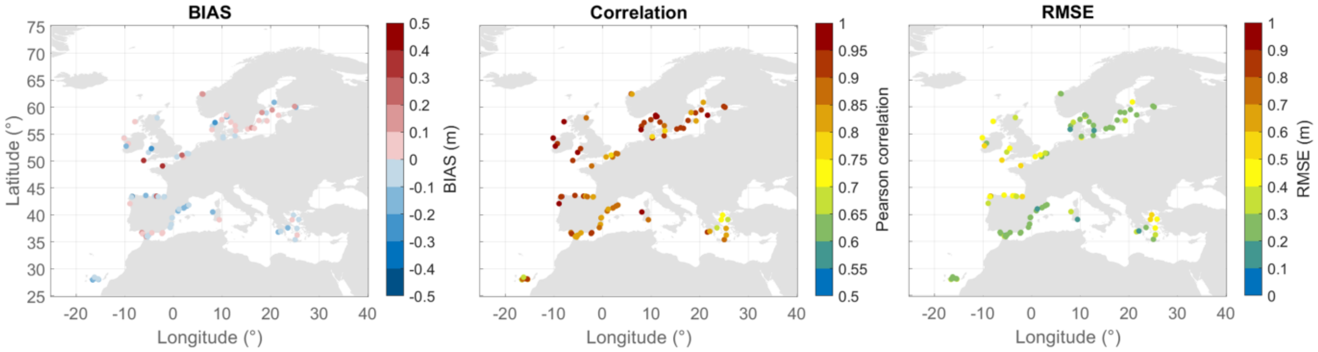

Figure S5: Spatial distribution of bias (left), Pearson correlation (middle), and RMSE (right) in significant wave height (Hs, m) from the nearshore wave hindcast, evaluated at the locations of coastal wave buoys.

Sensitivity analysis: selection of nodes within marine dynamics databases

A sensitivity analysis was performed to assess how the data selection with nearest grid point as opposed to interpolation influence the P95 results of astronomical tide, storm surge, and TWL in a selection of CTPs. The nearest grid point was selected based on the closest node of each database to the CTP at hand. The interpolation method was based on a linear interpolation with nearest-neighbor extrapolation. Figure S6 presents the results for three locations, one in each of the three European regions identified in the study. The largest differences in astronomical tide and TWL are found in the Baltic Sea, while the largest differences in storm surge are found along the Atlantic coast. However, the statistical metrics analyzed indicate that such differences are too small to play a relevant role in the estimation of extreme values as R^2 range from 0.88 to 1, RMSE from 0 to 0.002 m, and bias from -0.001 to 0.001. Therefore, the different results obtained with both approaches do not justify the use of interpolation methods in this case, particularly at this scale, when there are 51,010 points in which the method is required.

Therefore, when selecting the astronomical tide and storm surge data, the nearest grid point approach was adopted instead of interpolation for its computational efficiency after ensuring that such a decision has no influence on the results. We highlight that the resolution of the different databases is higher than the resolution at which such variables usually vary. The astronomical tide TPXO spatial resolution is around 3.5 km and the storm surge spatial resolution is 10 – 15 km. Meanwhile, astronomical tide and storm surge processes present a spatial variability of approximately hundreds to thousands of kilometers (Woodworth et al., 2019). Therefore, the resolution of the databases used provide a sufficiently dense sampling to capture their regional gradients.

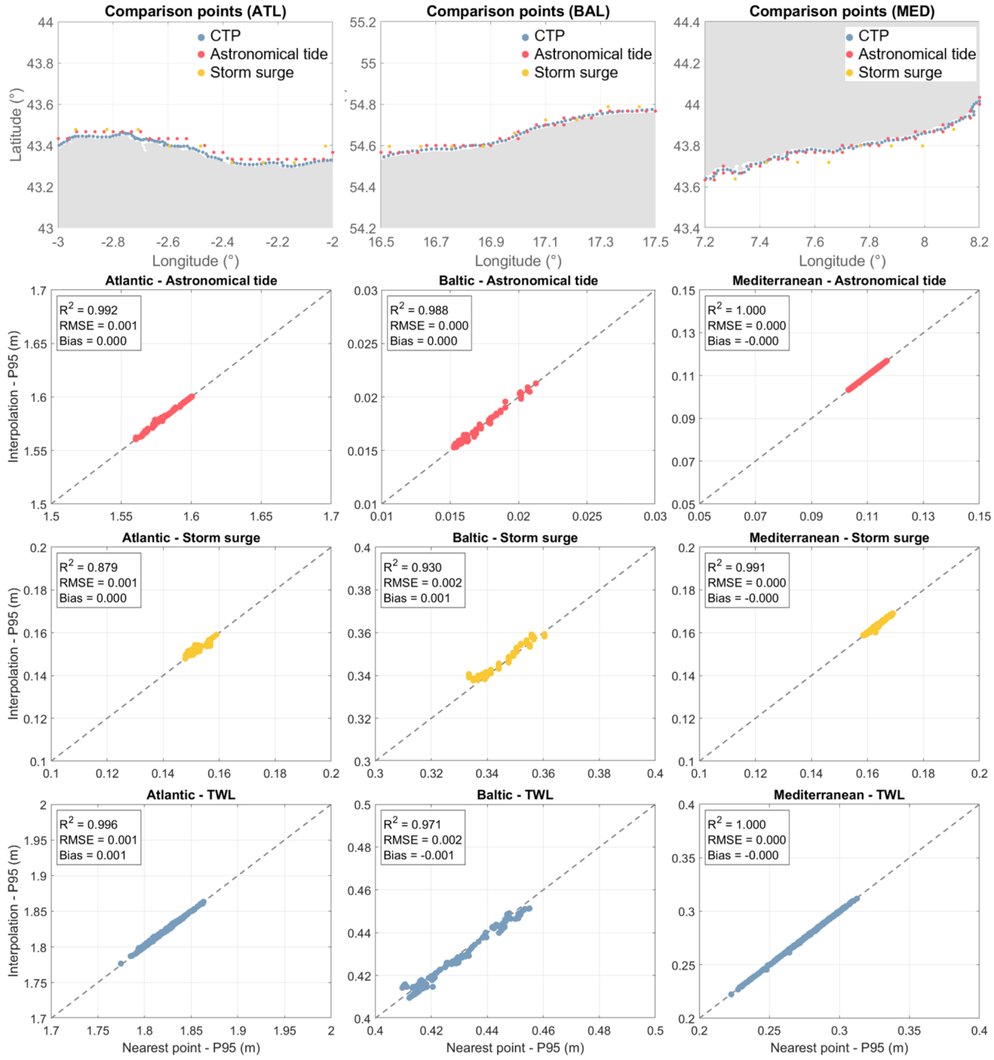

Comparison points (ATL)

Comparison points (BAL)

Comparison points (MED)

Atlantic - Astronomical tide

Baltic - Astronomical tide

Mediterranean - Astronomical tide

Atlantic - Storm surge

Baltic - Storm surge

Mediterranean - Storm surge

Atlantic - TWL

Baltic - TWL

Mediterranean - TWL

Figure S6: Sensitivity analysis of selection of corresponding marine database information based on P95. Examples are shown for smaller areas located in each of the three European regions identified in the study: Atlantic coast (left column), Baltic Sea (middle column), and Mediterranean Sea (right column).

Validation: foreshore slope

The foreshore slope is one of the main uncertainty sources in coastal flooding studies that consider wave contributions. Therefore, we validated the adopted approach to ensure its suitability at larger scales and identified the regions that are most sensitive to such variable.

The estimated foreshore slope data was validated with local-scale topography data and locally observed values for a series of sites across the study area. Figure S7 compares the foreshore slopes estimated with the Sunamura (1984) formulation against those obtained with a traditional method based on high-resolution data or field observations. The Sunamura formulation estimates foreshore slope as a spatially and temporally variable function of wave conditions. By contrast, the traditional method derives slopes from high-resolution DEM profiles (perpendicular to the coastline) in Sites 1 – 8, calculated as the intertidal slope between the mean low and high tides at each site. DEM data were obtained at the highest resolution available for the different sites (DEFRA, 2023; PDOK, 2023; IGN, 2021; IGN, 2019; Geoportale Emilia-Romagna, 2014). Meanwhile, the validation of Sites 9 – 12 was performed with locally observed slopes reported by previous studies (Nuyts et al., 2024; Carneiro-Barros et al. 2025); Jarmalavičius et al., 2025; McGlashan et al., 2004; respectively).

Overall, the different methods show good agreement, with the best agreements observed in Site 5, where the high-resolution DEM is in fact a topo-bathymetry allowing for a more precise slope estimate, and Site 9 where the reference slope was based on field observations of intertidal slope. The Sunamura formulation showed to be conservative (i.e., smoother slopes) in half of the sites used for validation. However, it is considered that the differences are small enough that they would not be reflected in the resulting extreme TWL estimations. The findings show that the Sunamura (1984) formulation is a robust method that performs well across diverse coastal settings, making it suitable for application at continental scale. Given that the traditional method requires field work or high-resolution topo-bathymetric data, which is not consistently available across Europe, the Sunamura approach represents a practical and sufficiently accurate alternative for defining foreshore slopes.

An identification of rocky coastlines has been conducted to acknowledge regions in which the misrepresentation of the foreshore slope could lead to a possible unrealistic estimation of the wave setup. According to EUROSION (2004), 16.7% of the study area is comprised of rocky cliffs, most of which is located along the United Kingdom (UK), Sweden, and Finland. Given the low wave climate energy in the Baltic Sea (Björkqvist et al., 2024), it is assumed that the possible inaccuracy of the foreshore slope in Sweden and Finland would likely not influence the extreme TWL results or the relative contributions of TWL components. Meanwhile, UK was included in the foreshore slope validation confirming its adequate representation.

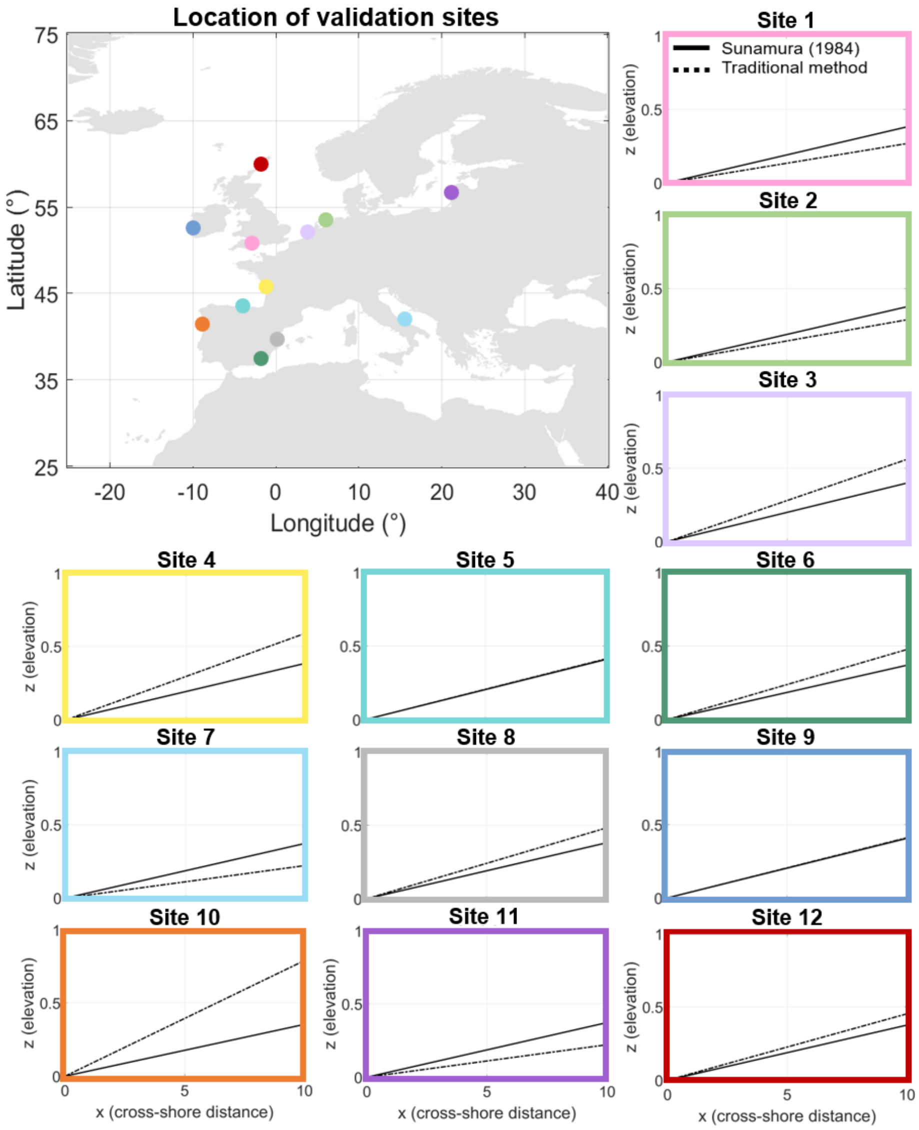

Figure S7: Comparison of mean foreshore slopes resulting from the Sunamura (1984) approach and a traditional method per site. Colored boxes refer to the location of sites shown in the map. The traditional slope values in Sites 1 – 8 were estimated with high-resolution DEM ranging from 1 m spatial resolution in Site 1 to 5 m in Site 2, for example. The traditional slope values in Sites 9 – 12 were obtained from local observations reported by previous studies.

Selection of test points with K-means

To facilitate the development of the methodology, a set of representative (test) points were selected using a K-means clustering technique (Camus et al., 2011) applied to the mean relative contributions of the TWL components. These points were only used in preliminary tests in EVA and served as graphical examples throughout the study.

Figure S8 displays the results of the clustering analysis, which does not isolate extreme events nor does it consider geographical location during its application. When adopting a 10-cluster selection (Figure S8a), it is possible to see a grouping of CTPs per European regions along the Atlantic coast (clusters 1, 4, 8, and 9), the Baltic Sea (clusters 2, 6, and 10), and the Mediterranean Sea (clusters 3, 5, and 7). Even though similar grouping patterns are observed with 100 clusters (Figure S8b) it is noticeable the smaller number of clusters in the Baltic Sea, in which only 10 clusters appear. Oppositely, the Atlantic coast presents 43 dominating clusters and the Mediterranean Sea, 47. The amount of clusters observed in each region provides an estimate of dominance, although clusters that are dominant in one region may still appear elsewhere at smaller frequencies. These results indicate that the Baltic Sea might be more homogeneous regarding the spatial variability of the marine climate drivers composing TWL than the two remaining regions.

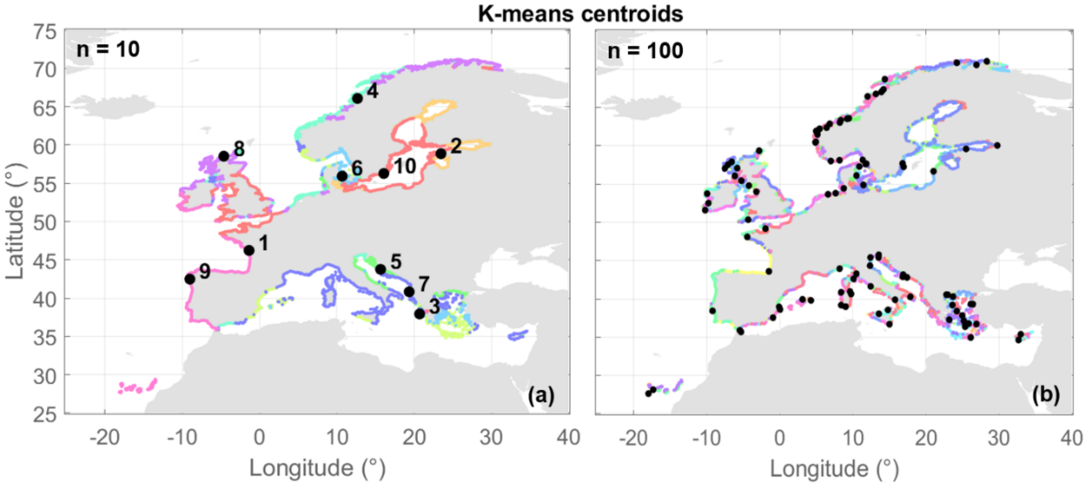

Figure S8: Selection of representative CTPs to be used in the EVA preliminary tests and as examples throughout this study. (a) Selection of 10 clusters with their respective centroids highlighted in black dots. (b) Selection of 100 clusters with their respective centroids highlighted in black dots (b). Results were generated with a k-means clustering based on relative contributions of TWL components under mean conditions.

Sensitivity analysis: POT threshold

Since the POT method is sensitive to the chosen threshold, which can introduce subjectivity and affect the results, a sensitivity analysis was needed to assess how robust and consistent the estimates are. Although the threshold selected in this study corresponds to a variable value corresponding to an average of two extremes events samples per year (λ=2) in each CTP, other options were tested.

Figure S9 presents a comparison of the EVA results when adopting a variable threshold corresponding to an average of 1 event per year (λ=1), 2 events (λ=2), or 3 events (λ=3). Although the corresponding TWL threshold varies up to 30%, the resulting 100-yr TWL varies up to 20% (Fig. 9a) and the corresponding 95th confidence interval up to 4%. The highest TWL threshold variabilities occur in the Baltic Sea, whereas the highest 100-yr TWL variabilities occur in the Mediterranean Sea. Meanwhile, the Atlantic coast is the least sensitive to the POT threshold selection. Figure S9b displays the results of the Anderson-Darling test when adopting the different POT thresholds. A rejected null-hypothesis provides evidence against the sample following an exponential distribution. Out of the 51,010 CTPs, only 121 CTPs indicate that none of the options lead to robust samples. The results shown for λ=1 and λ=2 are similar, with approximately 6.5% of the CTPs not adjusting well to an exponential fit. Meanwhile, λ=3 leads to more than double the number of CTPs rejecting the null hypothesis (15.3%). Figure S9c–d indicate which threshold tested leads to the highest and the lowest uncertainty as represented by the 95th confidence interval of the 100-yr TWL EVA results. Although, λ=1 indicates an overall good fit of the samples in the Anderson-Darling test, this is the threshold leading to the highest uncertainty of return levels. A possible explanation is that λ=1 leads to excessively small sample sizes, leading to instability in the EVA. Meanwhile, although adopting λ=3 yields the lowest uncertainty in most CTPs, the confidence interval difference between λ=2 and λ=3 remains below 1% for the majority of CTPs, indicating minimal impact for 73.3% of the CTPs.

Ultimately, there is no single threshold which solves the different challenges in all CTPs. However, given the poorer results from the Anderson-Darling test with λ=3, the higher uncertainties of the estimated return levels provided by λ=1, and the overall low 100-yr TWL variability across the different methods, λ=2 represents a reasonable balance between accuracy, robustness, and sample size to be used in EVA.

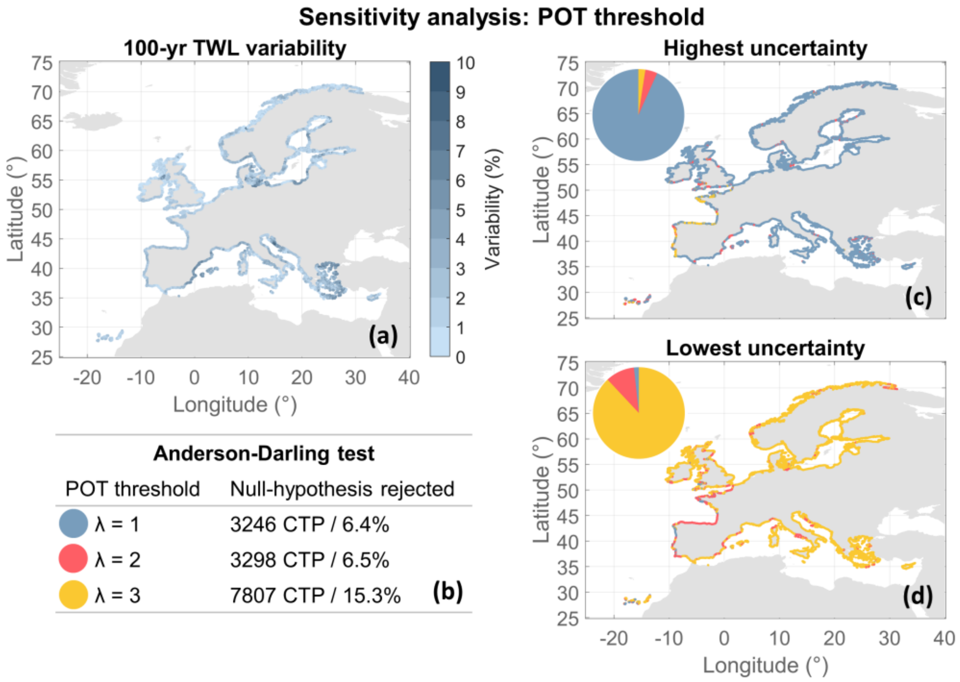

POT threshold	Null-hypothesis rejected
● λ = 1	3246 CTP / 6.4%
● λ = 2	3298 CTP / 6.5%
● λ = 3	7807 CTP / 15.3%

Figure S9: Sensitivity analysis of the POT threshold selected (λ=1 vs. λ=2 vs. λ=3). (a) Spatial distribution of the 100-yr TWL variability. (b) Anderson-Darling test results when adopting the different thresholds. A rejected null hypothesis provides evidence against the sample following an exponential fit. Uncertainty of results indicating which λ leads to (c) the highest and (d) the lowest uncertainties of return levels, based on the 95th confidence level.

Sensitivity analysis: POT interval

The interval used when declustering events to guarantee their independence can be spatially constant or variable, depending on local climatic characteristics. For example, for waves in the Atlantic Ocean, previous evidence suggests that a minimum interval of at least 3 days (or 72h) is required, even though the Poisson assumption is well satisfied with intervals up to 6 days (Méndez et al., 2006). Meanwhile, a storm surge study along the German Bight showed that the influence of the declustering time on the return level outcomes is minimal when adopting POT, compared to AM (Arns et al., 2013). Ultimately, in a POT analysis, the independence criterion should reflect the geophysical origin and duration of the extreme events under study. On the one hand, when defining a spatially constant value, the interval is well-established with 72h in storm surge studies (Caspers et al., 2025; Dullaart et al., 2023; MacPherson et al., 2019; Pupić Vurilj et al., 2025; Vousdoukas et al., 2016) although there are applications ranging from 1.5 days (Arns et al., 2013) to 6 days (Martín et al., 2024). In wave storm studies, a 48h interval has been commonly adopted (Lobeto et al., 2024) as well as a 12 – 24h calm period (Martzikos et al., 2023; Martzikos et al., 2021). On the other hand, spatially variable intervals have not been as explored, especially in large-scale studies. Similar to the adoption of a spatially variable POT threshold, the minimum interval would likely affect the estimation of return values as well as coastal flooding projections. However, the development of a methodology to define such heterogeneous interval values is out of the scope of the present study.

Following the decision of a spatially constant interval, a sensitivity analysis was performed to attest for the robustness of the adoption of the 72h instead of 48h and 96h. Figure S10 presents the EVA results obtained considering the different possibilities of declustering time. The 100-yr TWL variability resulting from the different POT minimum intervals tested is low compared to the other sensitivity analyses performed in this study (Figure S10a). The 95th confidence intervals of the 100-yr TWL indicate that 96h is the most uncertain option (Figure S10c), while 48h presents the lowest uncertainty (Figure S10d). However, the Anderson-Darling test analysis, indicates that the 72h interval leads to the highest proportion of CTPs adequately adjusting to the exponential fit (Figure S10b). Additionally, out of the 3298 CTPs in which the 72h interval does not result in robust distributions, 2098 CTPs rejected the null-hypothesis with all three POT minimum intervals tested.

The results indicate that, among the different steps of the methodology tested, the independence time between events has the least influence on the estimated return periods. Yet, this does not imply that the POT interval is irrelevant. Our analysis shows that it is still relevant, though less so than other methodological choices.

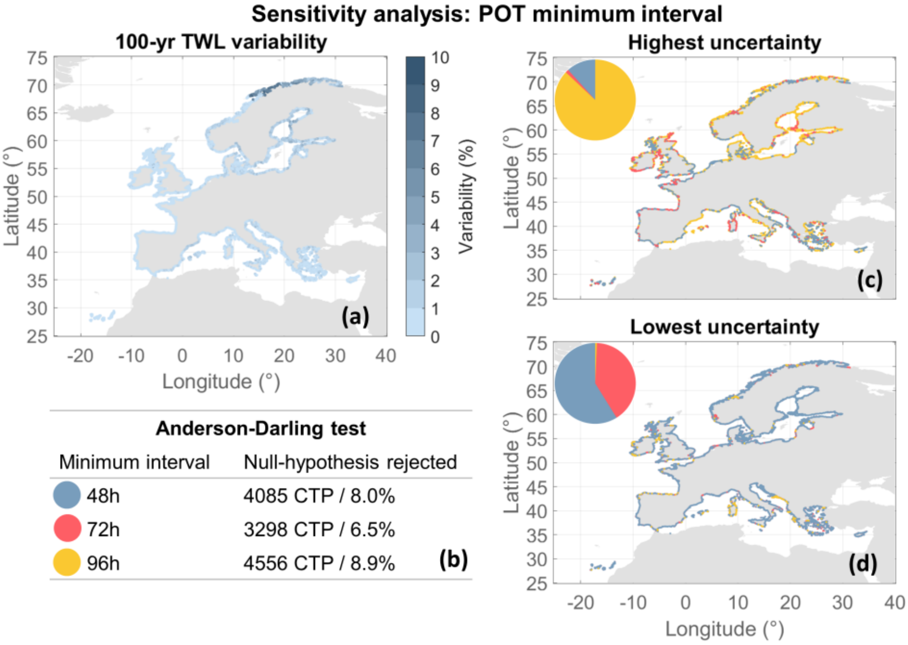

Minimum interval	Null-hypothesis rejected
● 48h	4085 CTP / 8.0%
● 72h	3298 CTP / 6.5%
● 96h	4556 CTP / 8.9%

Figure S10: Sensitivity analysis of the POT interval selected (48h vs. 72h vs. 96h). (a) Spatial variability 100-yr TWL variability. (b) Anderson-Darling test results when adopting the different intervals. A rejected null hypothesis indicates that the sample does not fit the exponential fit. Uncertainty of results indicating which interval leads to (c) the highest and (d) the lowest uncertainties of return levels, based on the 95th confidence level.

Sensitivity analysis: TWL resolution

The adoption of large-scale (offshore) wave conditions has been discussed throughout the study, while the effects of the TWL spatial resolution are examined in this sensitivity analysis. To this end, two alternative resolutions have been tested at spatial resolutions of 10 km and 25 km. In contrast to the 51,010 CTPs resulting from the 1 km resolution, these led to 4039 and 1324 CTPs, respectively. The goal of the analysis was to check whether this loss in TWL resolution and detail would affect the resulting 100-yr TWL and the corresponding flooded area (FA). Results from all three cases were compared based on the methodology adopted in this study: nearshore wave conditions, spatially variable foreshore slope, semi-empirical static wave setup, POT with λ=2, 72h minimum interval, and an exponential fit.

Table S3 displays the 100-yr TWL results per European basins and regions, based on the corresponding average and standard deviation values. For the entire study, the effect of the TWL resolution increases the more detail we add to the analysis. For example, for the entire study area, 100-yr TWL is 2.0 ± 1.3 m and 2.1 ± 1.4 m under 1 and 25 km spatial resolution, respectively. Meanwhile, in the Central Baltic Sea basin the 100-yr TWL changes from 1.4 ± 0.3 m with 1 km resolution to 1.7 ± 0.3 m with 25 km resolution. Overall, the higher the TWL resolution, the lower are the return values, indicating a possible overestimation of extreme TWL when lower resolution TWL is used instead. These results possibly represent a greater level of detail captured by the 1 km spatial resolution data as opposed to the one provided by 10 and 25 km resolutions.

For the European study area, the flooded areas vary by 0.5% and 1% when lowering the TWL resolution to 10 and 25 km, respectively. As with other analyses in this study, these values represent a balance of what occurs across different areas within the European floodplain. For example, in the Kattegat Bay the flooded area increases 0.5% with a lower TWL resolution, whereas in the NE Atlantic basin it decreases 14% with a 25 km resolution compared to the 1 km resolution adopted. In most basins, lower TWL resolution results in smaller flood extent. The most sensitive basins to the TWL resolution are located in the Atlantic region, which also showed to be the most sensitive region to the wave data selection in the sensitivity analysis of the wave setup components.

Table S3: Average ± standard deviation of 100-yr TWL (m) and the associated flooded area relative to the area of the corresponding floodplain (%) per European basin, region, and the entire study area. Results are shown for three scenarios of TWL spatial resolution: 1 km, 10 km, and 25 km.

EU basin / region	100-yr TWL (m)			100-yr relative FA (%)		
	1 km	10 km	25 km	1 km	10 km	25 km
Norway Sea	2.4 ± 0.4	2.5 ± 0.4	2.5 ± 0.4	35.0	35.0	35.0
NE Atlantic	3.9 ± 1.2	3.9 ± 1.1	4.0 ± 1.2	28.8	26.9	24.8
North Sea	3.5 ± 1.1	3.7 ± 1.1	3.6 ± 1.1	57.0	56.8	56.9
English Channel	5.1 ± 1.6	5.0 ± 1.7	5.0 ± 1.7	47.6	47.5	47.6
Iberia and Biscay	3.0 ± 0.6	3.0 ± 0.6	3.0 ± 0.6	34.2	33.9	33.5
Macaronesia	1.8 ± 0.2	1.9 ± 0.2	2.0 ± 0.2	12.3	12.0	11.3
Atlantic coast	**3.2 ± 1.2**	**3.3 ± 1.2**	**3.4 ± 1.3**	**49.4**	**49.0**	**48.8**
Kattegat Bay	1.7 ± 0.2	1.8 ± 0.2	1.9 ± 0.2	19.8	19.7	19.9
Central Baltic	1.4 ± 0.3	1.7 ± 0.3	1.7 ± 0.3	22.8	22.7	22.7
Gulfs	1.7 ± 0.3	1.9 ± 0.3	1.9 ± 0.3	17.3	17.3	17.3
Baltic Sea	**1.6 ± 0.3**	**1.8 ± 0.3**	**1.8 ± 0.3**	**20.7**	**20.6**	**20.6**
Central Mediterranean	0.7 ± 0.1	0.8 ± 0.1	0.8 ± 0.1	16.2	16.3	16.2
Ionian Sea	1.1 ± 0.2	1.1 ± 0.2	1.1 ± 0.3	11.1	11.0	11.0
Adriatic Sea	0.7 ± 0.1	0.8 ± 0.1	0.8 ± 0.2	37.1	37.0	37.0
Mediterranean Sea	**0.8 ± 0.2**	**0.9 ± 0.2**	**0.9 ± 0.2**	**24.4**	**24.3**	**24.3**
EUROPE	**2.0 ± 1.3**	**2.1 ± 1.4**	**2.1 ± 1.4**	**36.8**	**36.6**	**36.5**

Supplementary figures and table

Table S4: References used in the TWL reconstruction validation indicating the locations analyzed and the corresponding dates of the extreme events considered.

References	Location validated	Date of extreme event
Breilh et al. (2013)	Brouage (FR)	28/02/2010
Cabrita et al. (2024)	Porto Garibaldi (IT)	06/02/2015
IHCantabria (2021a)	Santander (ES)	03/03/2014
Irazoqui Apecechea et al. (2023)	Hoek van Holland (NL)	02 – 04/01/2018
	Huelva (ES)	26/02 – 05/03/2018
	Kiel (DE)	01 – 03/01/2019
	Marina Di Campo (IT)	27 – 30/10/2018
	Venice (IT)	11 – 18/11/2019
	Valencia (ES)	20 – 23/01/2020
Kiesel et al. (2023)	Koserow (DE)	02/01/2019
	Sassnitz (DE)	02/01/2019
	Schlei Fjord (DE)	02/01/2019
	Wismar (DE)	02/01/2019
	Klagshamn (SE)	02/01/2019
Koks et al. (2023)	Ebel Estuary (DE)	05 – 06/12/2013
Lemos et al. (2025)	Faro (PT)	04/01/2014
Perini et al. (2015)	Porto Corsini (IT)	06/02/2015
Scicchitano et al. (2021)	Catania (IT)	24 – 28/12/2009
	Catania (IT)	05 – 09/11/2014
	Catania (IT)	10 – 12/02/2015
	Portopalo di CapoPassero (IT)	27 – 28/09/2018
	Portopalo di CapoPassero (IT)	28 – 30/10/2016
	Portopalo di CapoPassero (IT)	11 – 12/11/2019
	Sicily (IT)	27 – 28/09/2018
	Malta (MT)	17 – 18/09/2020
Wadey et al. (2012)	Lymington (UK)	17/12/1989
	Solent (UK)	10/03/2008
Wolski & Wiśniewski (2021)	Wismar (DE)	20 – 23/11/2020
	Korsor (DK)	20 – 23/11/2020
	Parnu (EE)	20 – 23/11/2020
	Ristna (EE)	20 – 23/11/2020
	Hamina (FI)	20 – 23/11/2020
	Kemi (FI)	20 – 23/11/2020
	Swinoujscie (PL)	20 – 23/11/2020
	Skanor (SE)	20 – 23/11/2020
	Kungsholmsfort (SE)	20 – 23/11/2020

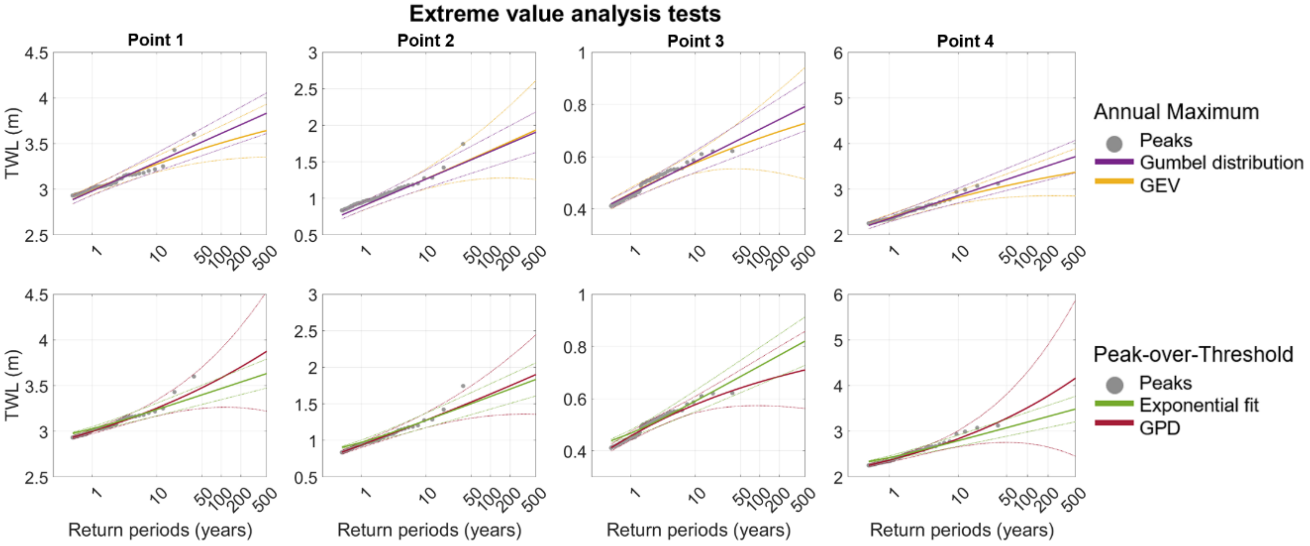

Figure S11: EVA tests performed for the first 10 centroids and shown for test points 1, 2, 3, and 4. Upper row shows results using annual maxima to select extreme events and distributions Gumbel and GEV to estimate return level events. Bottom row, peak-over-threshold with a threshold corresponding to a λ=2 and distributions exponential and GPD to estimate return levels.

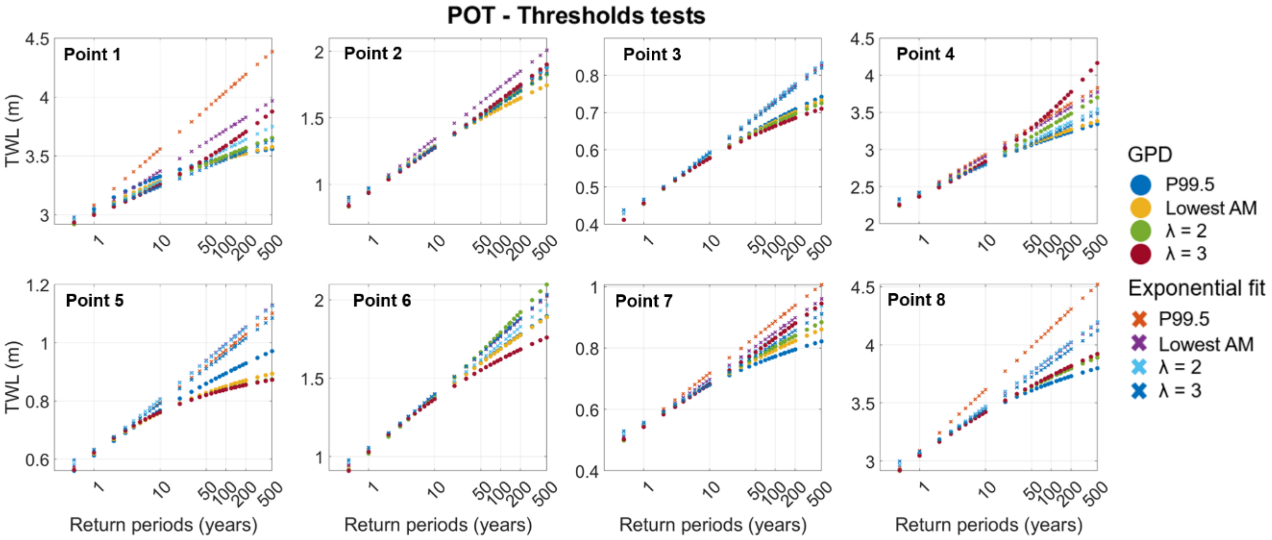

Figure S12: Threshold tests applied for the peak-over-threshold method when selecting the sample of exceedances (i.e., historic extremes events). Results are shown for both GPD and exponential fits for test points, 1, 2, 3, 4, 5, 6, 7, and 8.

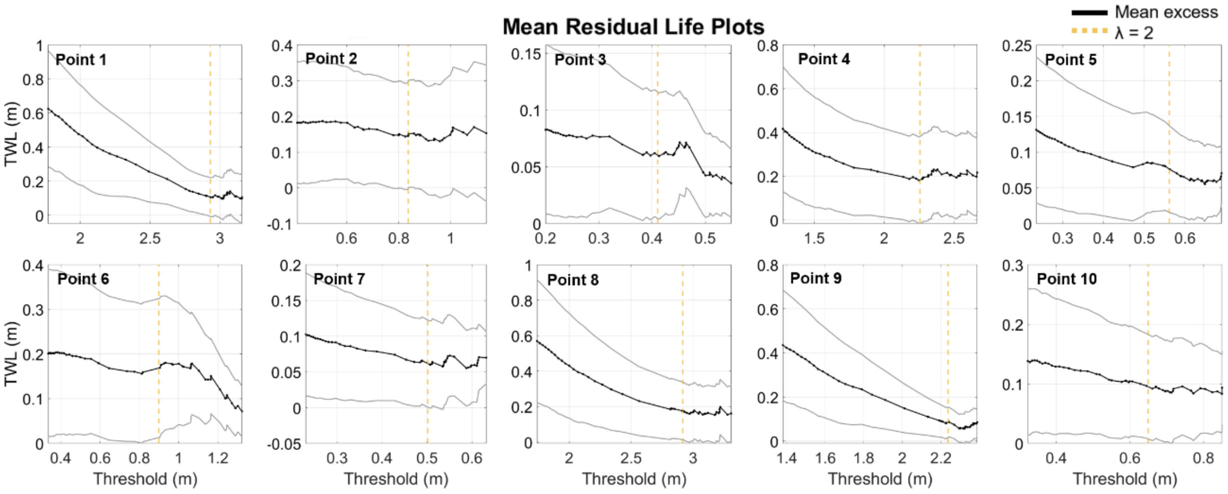

Figure S13: Mean residual life plots used to support the definition of a threshold for the POT method. Results are shown for the first 10 centroids used. Following Coles (2001), a stability in the plot indicates a potential value for a threshold. Yellow dashed lines indicate the TWL value correspondent to a λ=2, as proposed in the present study.

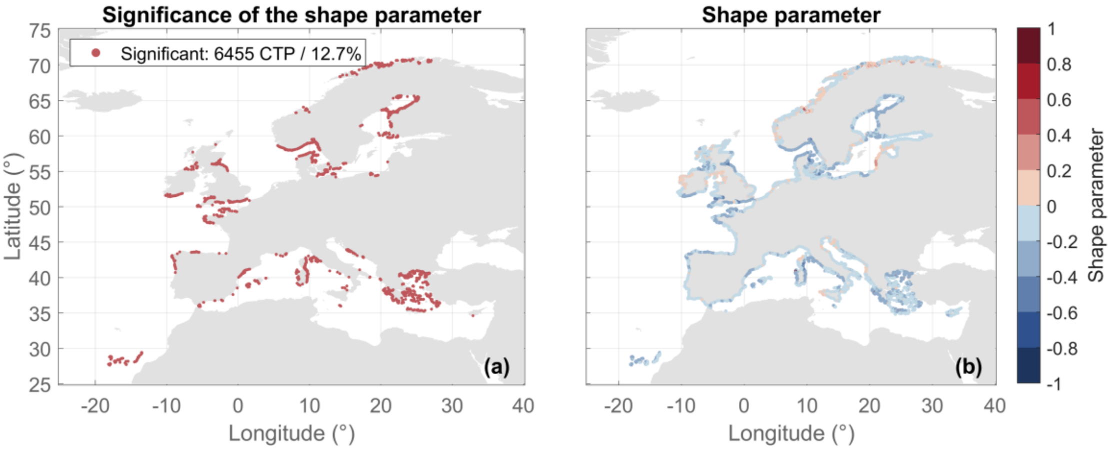

Figure S14: Spatial distribution of (a) the significancy of the Generalized Pareto Distribution (GPD) shape parameter and (b) the shape parameter.

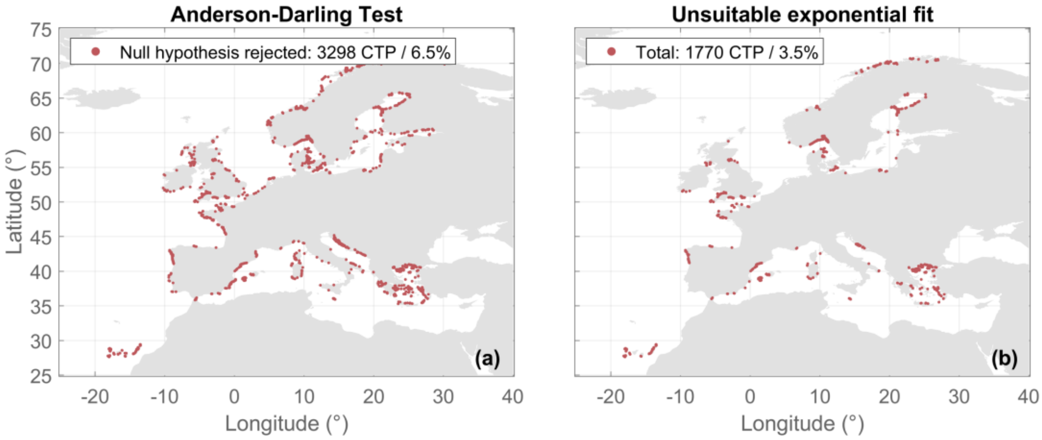

Figure S15: (a) Location of CTPs where the Anderson-Darling test resulted in a rejected null hypothesis, indicative of a poor fit to the exponential distribution. (b) Location of CTPs where the GPD shape parameter was significant and the Anderson-Darling test null hypothesis was rejected, indicating where the exponential fit was unsuitable to estimate return levels.

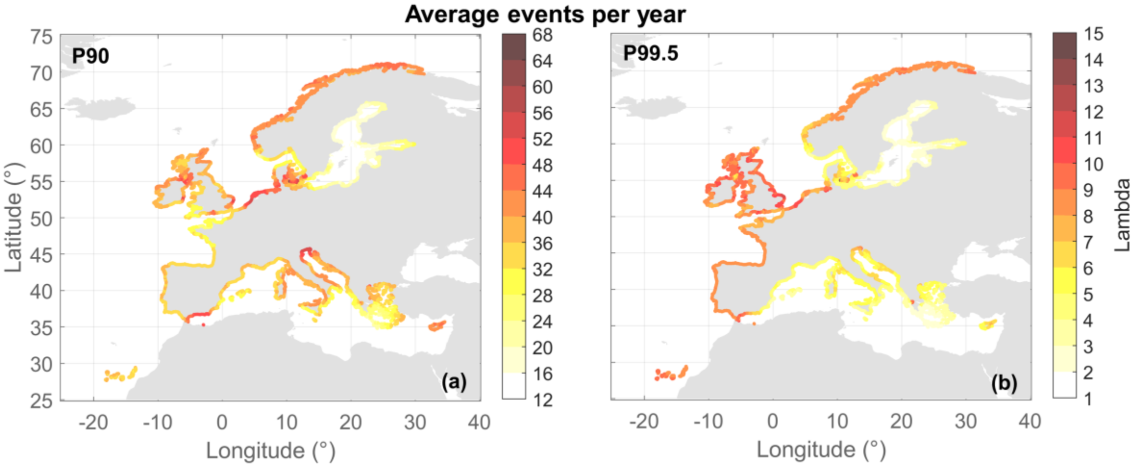

Figure S16: Spatial distributions of the λ (average events per year) resulting from a peak-over-threshold with a constant threshold of percentiles (a) P90 and (b) P99.5.

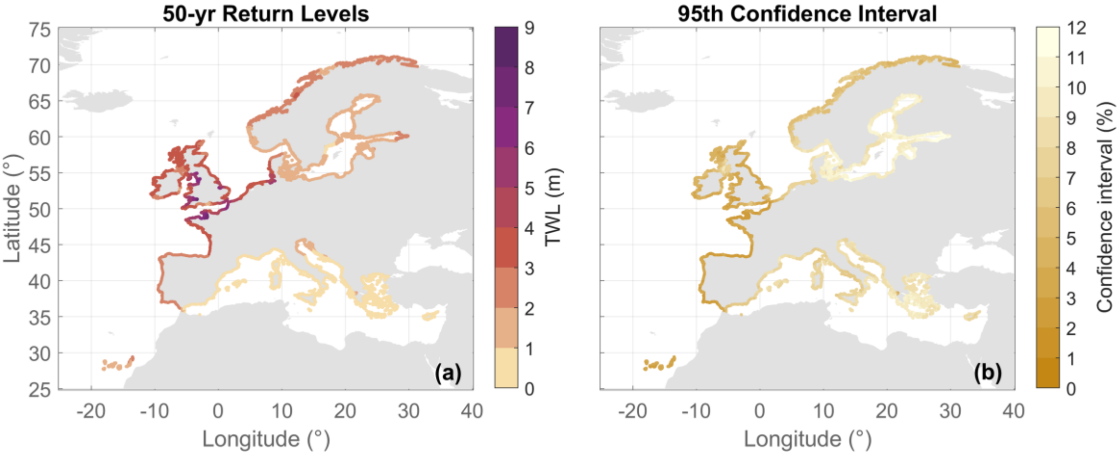

Figure S17: (a) Spatial distribution of the 50-yr return period TWL resulting from POT with an exponential fit and (b) spatial distribution of the 50-yr 95th confidence interval relative to the 50-yr TWL event, in percentage.

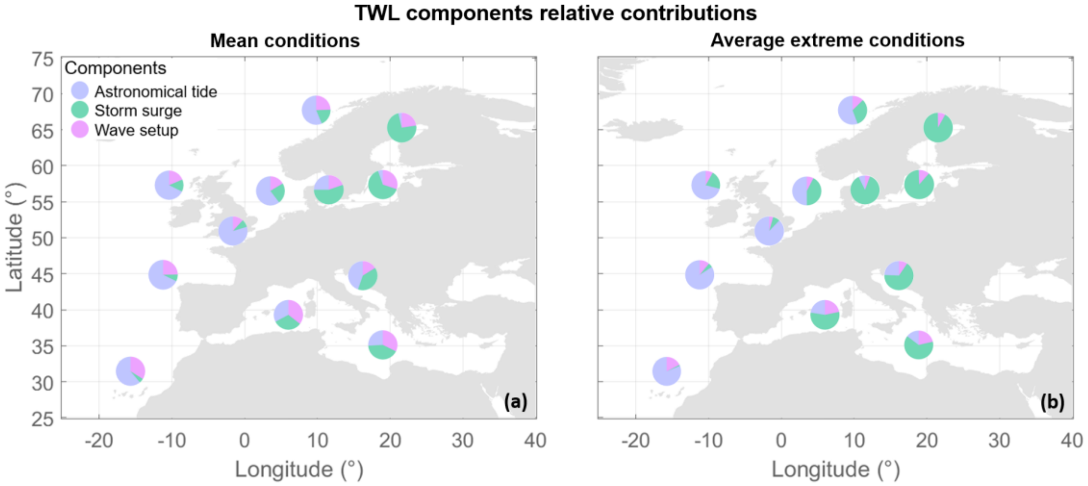

Figure S18: Average relative contributions of TWL components per European basin under (a) mean conditions and (b) extreme conditions.

References

Ardhuin, F., Rogers, E., Babanin, A. V., Filipot, J. F., Magne, R., Roland, A., van der Westhuysen, A., Queffeulou, P., Lefevre, J. M., Aouf, L., and Collard, F.: Semiempirical dissipation source functions for ocean waves. Part I: Definition, calibration, and validation, J. Phys. Oceanogr., 40, 1917–1941, https://doi.org/10.1175/2010JPO4324.1, 2010.

Arns, A., Wahl, T., Haigh, I. D., Jensen, J., and Pattiaratchi, C.: Estimating extreme water level probabilities: A comparison of the direct methods and recommendations for best practise, Coast. Eng., 81, 51–66, https://doi.org/10.1016/j.coastaleng.2013.07.003, 2013.

Björkqvist, J.-V., Kanarik, H., Tuomi, L., Niskanen, L., and Kankainen, M.: Event-based wave statistics for the Baltic Sea, State of the Planet, 4-osr8, 1–8, https://doi.org/10.5194/sp-4-osr8-10-2024, 2024.

Booij, N., Ris, R. C., and Holthuijsen, L. H.: A third-generation wave model for coastal regions 1. Model description and validation, J. Geophys. Res. Ocean., 104, 7649–7666, https://doi.org/10.1029/98JC02622, 1999.

Breilh, J. F., Chaumillon, E., Bertin, X., and Gravelle, M.: Assessment of static flood modeling techniques: Application to contrasting marshes flooded during Xynthia (western France), Nat. Hazards Earth Syst. Sci., 13, 1595–1612, https://doi.org/10.5194/nhess-13-1595-2013, 2013.

Cabrita, P., Montes, J., Duo, E., Brunetta, R., and Ciavola, P.: The Role of Different Total Water Level Definitions in Coastal Flood Modelling on a Low-Elevation Dune System, J. Mar. Sci. Eng., 12, 1003, https://doi.org/10.3390/jmse12061003, 2024.

Camus, P., Mendez, F. J., Medina, R., and Cofiño, A. S.: Analysis of clustering and selection algorithms for the study of multivariate wave climate, Coast. Eng., 58, 453–462, https://doi.org/10.1016/j.coastaleng.2011.02.003, 2011.

Camus, P., Mendez, F. J., Medina, R., Tomas, A., and Izaguirre, C.: High resolution downscaled ocean waves (DOW) reanalysis in coastal areas, Coast. Eng., 72, 56–68, https://doi.org/10.1016/j.coastaleng.2012.09.002, 2013.

Carneiro-Barros, J. E., Majidi, A. G., Plomaritis, T., Fazeres-Ferradosa, T., Rosa-Santos, P., and Taveira-Pinto, F.: Coastal Flooding Hazards in Northern Portugal: A Practical Large-Scale Evaluation of Total Water Levels and Swash Regimes, Water (Switzerland), 17, https://doi.org/10.3390/w17101478, 2025.

Caspers, J. J., Kindermann, P. E., Rongen, G. W. F., and Geerse, C. P. M.: Storm surge hydrographs and characteristics along the Dutch coast. An analysis from simulation data, Coast. Eng., 201, https://doi.org/10.1016/j.coastaleng.2025.104776, 2025.

Chapman, D. C.: Numerical treatment of cross-shelf open boundaries in a barotropic coastal ocean model, J. Phys. Oceanogr., 15, 1060–1075, https://doi.org/10.1175/1520-0485(1985)015<1060:NTOCSO>2.0.CO;2, 1985.

Chawla, A. and Tolman, H. L.: Obstruction grids for spectral wave models, Ocean Model., 22, 12–25, https://doi.org/10.1016/j.ocemod.2008.01.003, 2008.

Chen, T. C., Collet, F., and Di Luca, A.: Evaluation of ERA5 precipitation and 10-m wind speed associated with extratropical cyclones using station data over North America, Int. J. Climatol., 44, 729–747, https://doi.org/10.1002/joc.8339, 2024.

Cid, A., Castanedo, S., Abascal, A. J., Menéndez, M., and Medina, R.: A high resolution hindcast of the meteorological sea level component for Southern Europe: the GOS dataset, Clim. Dyn., 43, 2167–2184, https://doi.org/10.1007/s00382-013-2041-0, 2014.

Codiga, D. L.: Unified Tidal Analysis and Prediction Using the UTide Matlab Functions, 59, https://doi.org/10.13140/RG.2.1.3761.2008, 2011.

DEFRA, Department for Environment, Food & Rural Affairs: LIDAR Composite Digital Terrain Model (DTM). Available at: https://environment.data.gov.uk/dataset/13787b9a-26a4-4775-8523-806d13af58fc (last access: 22 April 2026), 2023.

Dullaart, J. C. M., Muis, S., De Moel, H., Ward, P. J., Eilander, D., and Aerts, J. C. J. H.: Enabling dynamic modelling of coastal flooding by defining storm tide hydrographs, Nat. Hazards Earth Syst. Sci., 23, 1847–1862, https://doi.org/10.5194/nhess-23-1847-2023, 2023.

Egbert, G. D. and Erofeeva, S. Y.: Efficient inverse modeling of barotropic ocean tides, J. Atmos. Ocean. Technol., 19, 183–204, https://doi.org/10.1175/1520-0426(2002)019<0183:EIMOBO>2.0.CO;2, 2002.

Egbert, G. D., Bennett, A. F., and Foreman, M. G. G.: TOPEX/POSEIDON tides estimated using a global inverse model, J. Geophys. Res., 99, https://doi.org/10.1029/94jc01894, 1994.

EUROSION: Living with Coastal Erosion in Europe: Sediment and Space for Sustainability. Part-1 Major Findings and Policy Recommendations of the EUROSION Project. Guidelines for implementing local information systems dedicated to coastal erosion management. Service , 54 pp., http://www.eurosion.org/ (last access: 23 April 2026), 2004.

Flather, R. A.: A tidal model of the northwest European continental shelf, Mem. Soc. Roy. Sci. Liege, 10(6), 141–164, 1976.

Geoportale Emilia-Romagna, R.-R: DTM 5x5. Available at: https://geoportale.regione.emilia-romagna.it/catalogo/dati-cartografici/altimetria/layer-2 (last access: 22 April 2026), 2014.

Haigh, I. D., Marcos, M., Talke, S. A., Woodworth, P. L., Hunter, J. R., Hague, B. S., Arns, A., Bradshaw, E., and Thompson, P.: GESLA Version 3: A major update to the global higher-frequency sea-level dataset, Geosci. Data J., 10, 293–314, https://doi.org/10.1002/gdj3.174, 2022.

Hersbach, H., Bell, B., Berrisford, P., Hirahara, S., Horányi, A., Muñoz-Sabater, J., Nicolas, J., Peubey, C., Radu, R., Schepers, D., Simmons, A., Soci, C., Abdalla, S., Abellan, X., Balsamo, G., Bechtold, P., Biavati, G., Bidlot, J., Bonavita, M., De Chiara, G., Dahlgren, P., Dee, D., Diamantakis, M., Dragani, R., Flemming, J., Forbes, R., Fuentes, M., Geer, A., Haimberger, L., Healy, S., Hogan, R. J., Hólm, E., Janisková, M., Keeley, S., Laloyaux, P., Lopez, P., Lupu, C., Radnoti, G., de Rosnay, P., Rozum, I., Vamborg, F., Villaume, S., and Thépaut, J. N.: The ERA5 global reanalysis, Q. J. R. Meteorol. Soc., 146, 1999–2049, https://doi.org/10.1002/qj.3803, 2020.

IGN, Instituto Geográfico Nacional: Modelo Digitial del Terreno (5 metros) de España. Available at: https://www.ign.es/web/ign/portal/cbg-area-cartografia (last access: 22 April 2026), 2019.

IGN, Institut National de L'Information Géographic et Forestiere: RGE Alti. Available at: https://geoservices.ign.fr/rgealti (last access: 22 April 2026), 2021.

IHCantabria, Instituto de Hidráulica Ambiental de Cantabria: Elaboración de la evaluación de impactos y riesgos de inundación y erosión debidos al cambio climático en la costa murciana. Available at: https://pimamurcia.ihcantabria.es/visor/#datos (last access: 23/04/2026), 2021.

Irazoqui Apecechea, M., Melet, A., and Armaroli, C.: Towards a pan-European coastal flood awareness system: Skill of extreme sea-level forecasts from the Copernicus Marine Service , 2023.

Jarmalavičius, D., Žilinskas, G., Pupienis, D., and Janušaitė, R.: Resilience of beach morphometric characteristics on decadal time scale: a case study from the Lithuanian Baltic Sea, Oceanol. Polish Acad. Sci., 67, https://doi.org/https://doi.org/10.5697/KSMY5385, 2025.

Kiesel, J., Lorenz, M., König, M., Gräwe, U., and Vafeidis, A. T.: Regional assessment of extreme sea levels and associated coastal flooding along the German Baltic Sea coast, Nat. Hazards Earth Syst. Sci., 23, 2961–2985, https://doi.org/10.5194/nhess-23-2961-2023, 2023.

Koks, E. E., Le Bars, D., Essenfelder, A. H., Nirandjan, S., and Sayers, P.: The impacts of coastal flooding and sea level rise on critical infrastructure: a novel storyline approach, Sustain. Resilient Infrastruct., 8, 237–261, https://doi.org/10.1080/23789689.2022.2142741, 2023.

Lemos, G., Soares, P. M. M., Simões, R., Antunes, C., Bosnic, I., and Pinto, C.: A physical climate storyline for the Hercules storm in Portugal: Extreme coastal flooding in southwestern Europe under a changing climate, Sci. Total Environ., 971, https://doi.org/10.1016/j.scitotenv.2025.179050, 2025.

Lobeto, H., Semedo, A., Lemos, G., Dastgheib, A., Menendez, M., Ranasinghe, R., and Bidlot, J.-R.: Global coastal wave storminess, Sci. Rep., 14, https://doi.org/10.1038/s41598-024-51420-0, 2024.

MacPherson, L. R., Arns, A., Dangendorf, S., Vafeidis, A. T., and Jensen, J.: A Stochastic Extreme Sea Level Model for the German Baltic Sea Coast, J. Geophys. Res. Ocean., 124, 2054–2071, https://doi.org/10.1029/2018JC014718, 2019.

Martín, A., Wahl, T., Enriquez, A. R., and Jane, R.: Storm surge time series de-clustering using correlation analysis, Weather Clim. Extrem., 45, https://doi.org/10.1016/j.wace.2024.100701, 2024.

Martzikos, N., Malliouri, D., and Tsoukala, V.: Shape investigation and probabilistic representation of coastal storms. Applications to Mykonos and Barcelona, Appl. Ocean Res., 135, https://doi.org/10.1016/j.apor.2023.103563, 2023.

Martzikos, N. T., Prinos, P. E., Memos, C. D., and Tsoukala, V. K.: Statistical analysis of Mediterranean coastal storms, Oceanologia, 63, 133–148, https://doi.org/10.1016/j.oceano.2020.11.001, 2021.

McGlashan, D. J., Duck, R. W., and Reid, C. T.: The foreshore: Geographical implications of the three legal systems in Great Britain, Area, 36, 338–347, https://doi.org/10.1111/j.0004-0894.2004.00235.x, 2004.

Méndez, F. J., Menéndez, M., Luceño, A., and Losada, I. J.: Estimation of the long-term variability of extreme significant wave height using a time-dependent Peak Over Threshold (POT) model, J. Geophys. Res. Ocean., 111, 1–13, https://doi.org/10.1029/2005JC003344, 2006.

Nuyts, S., Farrell, E. J., Fennell, S., and Nash, S.: An Assessment of the Role of the Timex Sampling Strategy on the Precision of Shoreline Detection Analysis, Coasts, 4, 347–365, https://doi.org/10.3390/coasts4020018, 2024.

PDOK, Publieke Dienstverlening Op de Kaart: Current Elevation Model Netherlands (AHN). Available at: https://www.pdok.nl/ (last access: 23 April 2026), 2023.

Perini, L., Calabrese, L., Lorito, S., and Luciani, P.: Il rischio da mareggiata in Emilia-Romagna: l'evento del 5-6 Febbraio 2015, Geol. Vol., 53, 8–17. https://www.researchgate.net/publication/301219671_Il_rischio_da_mareggiata_in_Emilia-Romagna_l'evento_del_5-6_febbraio_2015 (last access: 23 April 2026), 2015.

Pupić Vurilj, M., Antolínez, J. A. Á., Muis, S., and Morales Napoles, O.: Storm surge hydrographs from historical observations of sea level along the Dutch North Sea coast, Nat. Hazards, https://doi.org/10.1007/s11069-025-07351-8, 2025.

Rogers, W. E. R. and Linzell, R. S.: The IRI Grid System for Use with WAVEWATCH III®, NRL Memorandum Report, 47. Available at: https://apps.dtic.mil/sti/citations/AD1065566 (last access: 23 April 2026), 2018.

Scicchitano, G., Scardino, G., Monaco, C., Piscitelli, A., Milella, M., De Giosa, F., and Mastronuzzi, G.: Comparing impact effects of common storms and Medicanes along the coast of south-eastern Sicily, Mar. Geol., 439, 106556, https://doi.org/10.1016/j.margeo.2021.106556, 2021.

Shchepetkin, A. F. and McWilliams, J. C.: The regional oceanic modeling system (ROMS): A split-explicit, free-surface, topography-following-coordinate oceanic model, Ocean Model., 9, 347–404, https://doi.org/10.1016/j.ocemod.2004.08.002, 2005.

Stopa, J. E.: Wind forcing calibration and wave hindcast comparison using multiple reanalysis and merged satellite wind datasets, Ocean Model., 127, 55–69, https://doi.org/10.1016/j.ocemod.2018.04.008, 2018.

Sunamura, T.: Quantitative Predictions of Beach-Face Slopes., Bull. Geol. Soc. Am., 95, 242–245, https://doi.org/10.1130/0016-7606(1984)95<242:qpobs>2.0.co;2, 1984.

Tolman, H. L.: User manual and system documentation of WAVEWATCH-IIITM version 3.14, Department of Commerce, National Oceanic and Atmospheric Administration, National Centers for Environmental Prediction, Marine Modeling and Analysis Branch Technical Note No. 276. Available at: https://polar.ncep.noaa.gov/mmab/papers/tn276/MMAB_276.pdf (last access: 23 April 2026), 2009.

Vousdoukas, M. I., Voukouvalas, E., Annunziato, A., Giardino, A., and Feyen, L.: Projections of extreme storm surge levels along Europe, Clim. Dyn., 47, 3171–3190, https://doi.org/10.1007/s00382-016-3019-5, 2016.

Wadey, M. P., Nicholls, R. J., and Hutton, C.: Coastal flooding in the solent: An integrated analysis of defences and inundation, Water (Switzerland), 4, 430–459, https://doi.org/10.3390/w4020430, 2012.

Wolski, T. and Wiśniewski, B.: Characteristics and long-term variability of occurrences of storm surges in the baltic sea, Atmosphere (Basel)., 12, https://doi.org/10.3390/atmos12121679, 2021.

Woodworth, P. L., Melet, A., Marcos, M., Ray, R. D., Wöppelmann, G., Sasaki, Y. N., Cirano, M., Hibbert, A., Huthnance, J. M., Monserrat, S., and Merrifield, M. A.: Forcing Factors Affecting Sea Level Changes at the Coast, Springer Netherlands, 1351–1397 pp., https://doi.org/10.1007/s10712-019-09531-1, 2019.

WW3DG, The WAVEWATCH III® Development Group (WW3DG): User manual and system documentation of WAVEWATCH III® version 6.07. Tech. Note 333, NOAA/NWS/NCEP/MMAB, College Park, MD, USA, 465 pp. + Appendices. Available at: https://data-ww3.ifremer.fr/COURS/WAVES_SHORT_COURSE/MODEL/manual.pdf (last access: 23 April 2026), 2019.